nature photonics

Article

https://doi.org/10.1038/s41566-024-01383-5

Efficient and stable perovskite solar cells with regulated depletion region

Received: 7 February 2023

Accepted: 4 January 2024

Published online: 12 February 2024

Check for updates

Zhichao Shen[1,5], Qifeng Han[1,5] ✉, Xinhui Luo[1], Yangzi Shen[1], Yanbo Wang[1], Yongbo Yuan[2], Yiqiang Zhang[3], Yang Yang[4] ✉ & Liyuan Han[1] ✉

Irreversible ion migration from the perovskite layer to the charge transport layer and metal electrodes causes irreversible efficiency loss in perovskite solar cells. Confining the mobile ions within the perovskite layer is a promising strategy to improve the long-term operational stability of solar cells. Here we inhibit the migration of iodide ions out of the perovskite under light illumination by creating a depletion region inside the perovskite layer. Precise control of the doping depth induces an electric field within the perovskite that counteracts ion migration while enhancing carrier separation. Our devices exhibit a certified power conversion efficiency of 24.6% and maintain over 88% of the initial efficiency after 1,920 h of continuous illumination under maximum power point conditions (65 °C in ambient air, following the ISOS-L-2 protocol). The power conversion efficiency returns to more than 94% of its initial value after overnight recovery. When operating under repeated 12 h light on/off cycles for over 10,000 h (solar simulator at 65 °C and ambient air, following the ISOS-LC-2 protocol), the efficiency loss is less than 2%. We expect this method to open up new and effective avenues towards enhancing the long-term stability of high-performance perovskite photovoltaics.

The power conversion efficiency (PCE) of perovskite solar cells (PSCs) has developed rapidly over the past decade[1–7], with a certified efficiency of 26.1% obtained[8]. Realizing long-term stability on highly efficient PSCs is an important prerequisite for commercialization. Despite many efforts to improve the stability of PSCs, ion migration under light illumination remains a major issue that impairs their operational stability[9–11]. There are reversible and irreversible ion migrations in PSCs: the former occurs inside the perovskite layer, which hardly affects the performance under real work condition because the performance can almost recover to initial values at night[12–14], whereas the latter involves ions migrating out of the perovskite layer and into the carrier transport layer (CTL) or electrode, permanently damaging device performance[15–17]. The incorporation of migrated ions into the CTL causes energy disorder and even affects the CTL conductivity type, resulting in rapid performance degradation[16,17]. Rear electrodes such as silver and aluminium react with migrated halide anions to form resistive compounds, reducing carrier collection ability[18,19].

Many methods—such as composition engineering[20,21], additive engineering[22,23] and interface engineering—have been developed to suppress irreversible ion migration[17,24–26]. Among them, interface engineering has attracted wide attention and can be divided into two categories: passivating surface defects and inserting a barrier layer. Surface passivation using alkylammonium halide salts and Lewis acid–base materials reduces ion migration channels[25,27], and polymer, graphene or inorganic oxide is deposited onto the perovskite layer as a barrier layer to block ion migration[17,19,26]. However, these interface-blocking methods

[1]State Key Laboratory of Metal Matrix Composites, Shanghai Jiao Tong University, Shanghai, China. [2]Hunan Key Laboratory of Super-microstructure and Ultrafast Process, School of Physics and Electronics, Central South University, Changsha, China. [3]School of Materials Science and Engineering, Henan Institute of Advanced Technology, Zhengzhou University, Zhengzhou, China. [4]Department of Materials Science and Engineering and California NanoSystems Institute, University of California Los Angeles, Los Angeles, CA, USA. [5]These authors contributed equally: Zhichao Shen, Qifeng Han. ✉e-mail: Han.qifeng@sjtu.edu.cn; yangy@ucla.edu; han.liyuan@sjtu.edu.cn

only passively mitigate ion migration. The ions will still continuously migrate to the heterointerface and unstoppably diffuse into the CTL, especially under long-term illumination due to the high concentration gradient and large amount of ion migration channels on the surface[19]. A proactive technique to limit ion migration inside the perovskite absorption layer is therefore essential to achieve intrinsically stable PSCs.

The built-in electric field at the depletion region, which can drive mobile ions against diffusion, is usually located at the heterointerface between the CTL and the perovskite layer[28–30]. When illuminated, the photo-induced electric field promotes the iodide ions inside of the perovskite layer to strongly migrate towards the heterointerface; they will then continuously and irreversibly diffuse into a hole transport layer (HTL) such as 2,2′,7,7′-tetrakis(*N*,*N*-di p-methoxyphenylamine)-9,9′-spirobifluorene (spiro-OMeTAD) or poly(bis(4-phenyl)(2,4,6-trimethylphenyl) amine) (PTAA) due to the large concentration gradient and plethora of ion migration channels at the heterointerface. To intrinsically suppress irreversible ion migration, it is essential to move the depletion region into the perovskite layer to prevent ions from migrating to the interface.

Here we successfully regulated the depletion region into the perovskite layer by precisely controlling the depth of dopant to alter the conductivity type of perovskite film. Therefore, a built-in electric field was created inside the perovskite layer, which can not only effectively block the migration of iodide ions away from HTL, but also enhance the carrier separation. As a result, we achieved a high certified PCE of 24.6% based on a PTAA device. The device maintained more than 88% of its initial efficiency after 1,920 h of continuous illumination under maximum power point (MPP) operating conditions (65 °C at ambient air following ISOS-L-2) and returned to more than 94% of its initial efficiency after overnight recovery in darkness. To simulate real working conditions, we conducted continuous interval illumination with 12 h light on/off (solar simulator/dark cycle at 65 °C and ambient air following ISOS-LC-2), and the PSCs can still maintain 98% of the initial efficiency after 10,000 h. When we replaced the PTAA by spiro-OMeTAD, we achieved a champion certified PCE of 25.2%, demonstrating the universality and effectiveness of our strategy.

Regulation strategy and characterization of depletion region

To regulate the depletion region inside of the perovskite layer, the capacity of dopants to remain in the perovskite film after high-temperature annealing is needed for favourable doping effects. The following criteria thus need to be considered: (1) the dopant can react with n-type defects Pb_I and V_I with low formation energy to realize effective doping (Pb_I means iodide site substitution by Pb while V_I means iodide vacancy)[31–33]; (2) the dopant can withstand a temperature of 150 °C to form a stable electric field inside the perovskite bulk; (3) extra ions are not introduced to prevent adverse effects on long-term stability; (4) the dopant is non-toxic and environmentally friendly; and (5) the dopant is preferably commercial and readily available. After preliminary screening, functional sweeteners are thus selected as dopants (Supplementary Fig. 1).

We sprayed the dopant onto perovskite precursor film before annealing (Supplementary Fig. 2). The dopants then penetrated into the porous structure of the perovskite precursor film (Supplementary Fig. 3). The formation of a porous structure is related to the fabrication process of PSCs, the details of which are described in the 'Perovskite solar cell fabrication' in Methods. The perovskite precursor films with dopants were then annealed at 150 °C to crystallize and form a stable depletion region. The differential scanning calorimetry and thermogravimetric analysis spectra were used to evaluate thermal stability of dopants (Supplementary Fig. 4). Aspartame was finally selected as the dopant because it can withstand a temperature of 150 °C. The system energy decreases by 1.915 eV and 1.878 eV when aspartame interacts with Pb_I and V_I, respectively, indicating a strong interaction between aspartame and the defects (Supplementary Fig. 5). Fourier-transform infrared spectroscopy and X-ray photoelectron spectroscopy (XPS) spectra further proved the interaction between aspartame and the defects in the perovskite film. A C=O stretching vibration frequency in pure aspartame is observed at 1,661 cm^{-1}, which shifts to 1,651 cm^{-1} (Supplementary Fig. 6) after interacting with the defects, and the peak from Pb 4*f* also shifts (Supplementary Fig. 7). Consequently, aspartame changed the perovskite conductivity type from n- to p-type because the reduced n-type defects no longer play the dominant role in deciding the conductivity type (Supplementary Figs. 8–11). By contrast, p-type defects play a decisive role (see Supplementary Note 1 for a detailed discussion).

According to the Darcy equation, the percolation coefficient is proportional to the density of the fluid and inversely proportional to the viscosity of the fluid[34–36]. Therefore, to accurately control the penetration depth of the dopant and then the location of the depletion region, we used solvents with varying density to viscosity ratios to dissolve the dopant: isopropanol (IPA), chlorobenzene (CB) and chloroform (CF), with ratios of 0.325, 1.389 and 2.664, respectively. The relevant parameters are summarized in Supplementary Table 1. We found when IPA or CB is used alone, the dopant can only exist on the shallow surface of perovskite at around 20 nm, because the density to viscosity ratio is too small. Although CF exhibits a large density to viscosity ratio, it volatilizes too quickly due to the large saturated vapour pressure. We therefore used mixed solvents to control the penetration depth. An XPS depth profile in Fig. 1a–c was used to detect the doping depth. When the etching time is 0 s, the XPS spectra show the elements at the surface, and the element analysis conducted after a different etching time shows the element distribution at a different depth. In this case, we detected an elemental tin signal after approximately 11,000 s of etching (Supplementary Fig. 12) indicating that the perovskite film had been completely etched. The perovskite film thickness is around 750 nm. For the sample treated by dopant with CB/CF = 3/7 mixed solvent, at the beginning of the etching process, we can obviously detect the oxygen signal, which belongs to the dopant aspartame. The oxygen signal is barely detectable after 1,500 s (Fig. 1a), indicating that the perovskite layer thickness with aspartame dopant is about 100 nm. Time-of-flight secondary-ion mass spectrometry (TOF-SIMS) was performed to confirm the XPS results, and they are consistent (Supplementary Fig. 13).

X-ray photoelectron spectra were also used to detect other dopant depths (Fig. 1b,c). The penetration depth of the dopant can be precisely controlled by adjusting the volume ratio of CB to CF and thus the ratio of density to viscosity (Supplementary Table 2). Besides, we found other mixed solvents with the same density viscosity ratio that can produce the same effect on the porous structure (Supplementary Figs. 14 and 15). The linear relationship between the density to viscosity ratio and the doping depth is shown in Fig. 1d. Furthermore, according to grazing-incidence X-ray diffraction from 0.5° to 2° and photoluminescence spectroscopy, there is no 2D layer formed on the perovskite surface after the doping process (Supplementary Figs. 16 and 17).

Fig. 1 | Characterization on the regulation of the depletion region. a–c, XPS depth profiles for samples with aspartame penetration depths of 100 nm (**a**), 50 nm (**b**) and 20 nm (**c**). In the early stages of the etching process, we performed XPS elemental analysis over long time intervals, which were then gradually narrowed down. **d**, The linear relationship between the density to viscosity ratio and the doping depth. **e**,**f**, KPFM of the cross-section profiles from control (**e**) and target (**f**) devices. Scale bars, 500 nm. The colour bar indicates the cross-section potential. The vertical dashed lines clearly distinguish between the FTO/SnO_2 layer, perovskite layer and HTL. The samples for KPFM were made on glass/FTO/SnO_2/perovskite/spiro-OMeTAD/Ag. The potential difference is obtained by subtracting the potential under the dark condition from that under illumination to eliminate the effect of static surface charge due to the cleaved surface.

https://doi.org/10.1038/s41566-024-01383-5

Kelvin probe force microscopy (KPFM) was used to detect the location of the depletion region. In our case, the depletion region locates between an n-type perovskite and a p-type HTL or perovskite. The depletion region of the p–n junction corresponds to the location at which potential change occurs. While near the perovskite/SnO_2 interface, the n–n junction was formed by a positive space charge

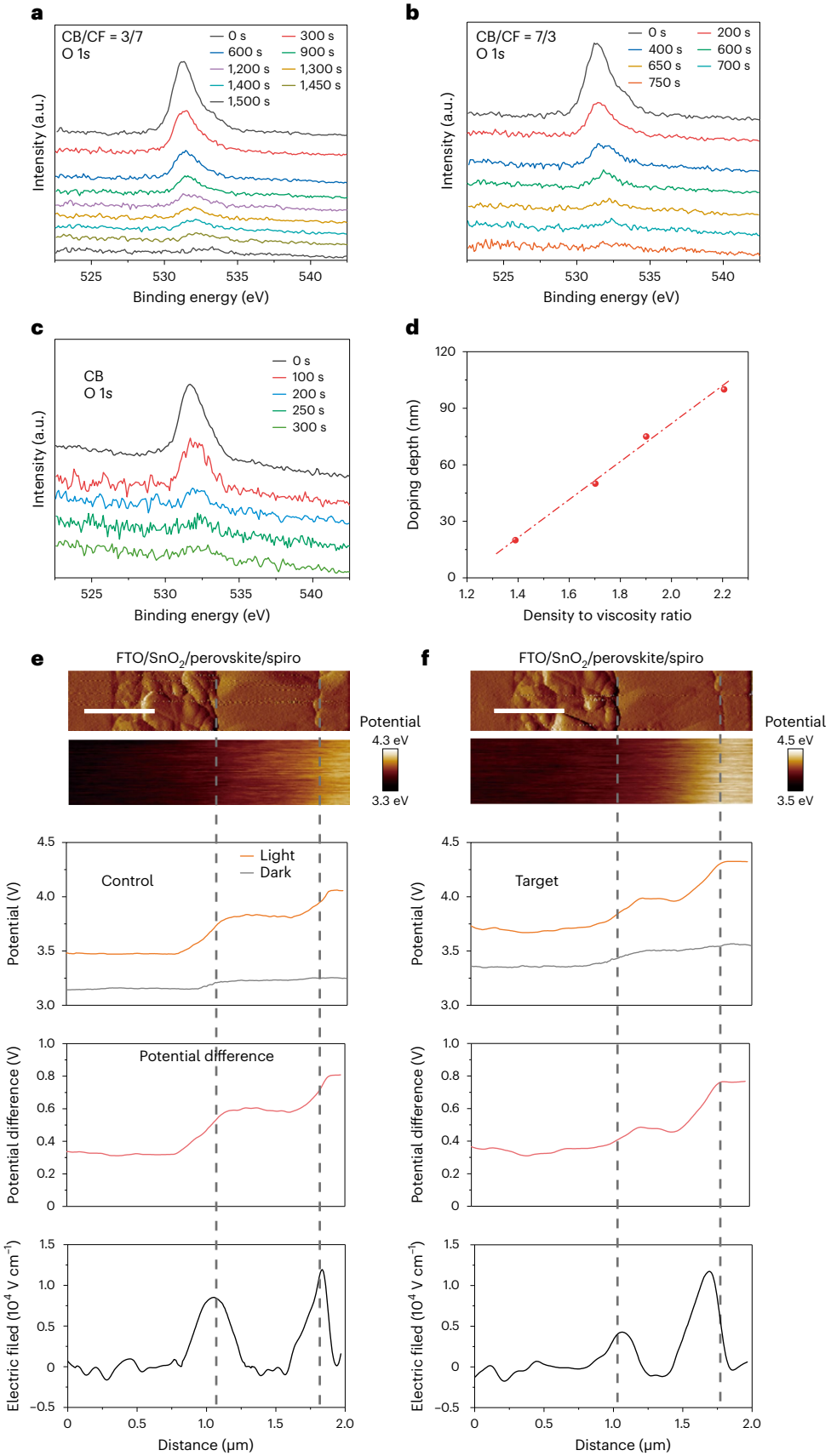

https://doi.org/10.1038/s41566-024-01383-5

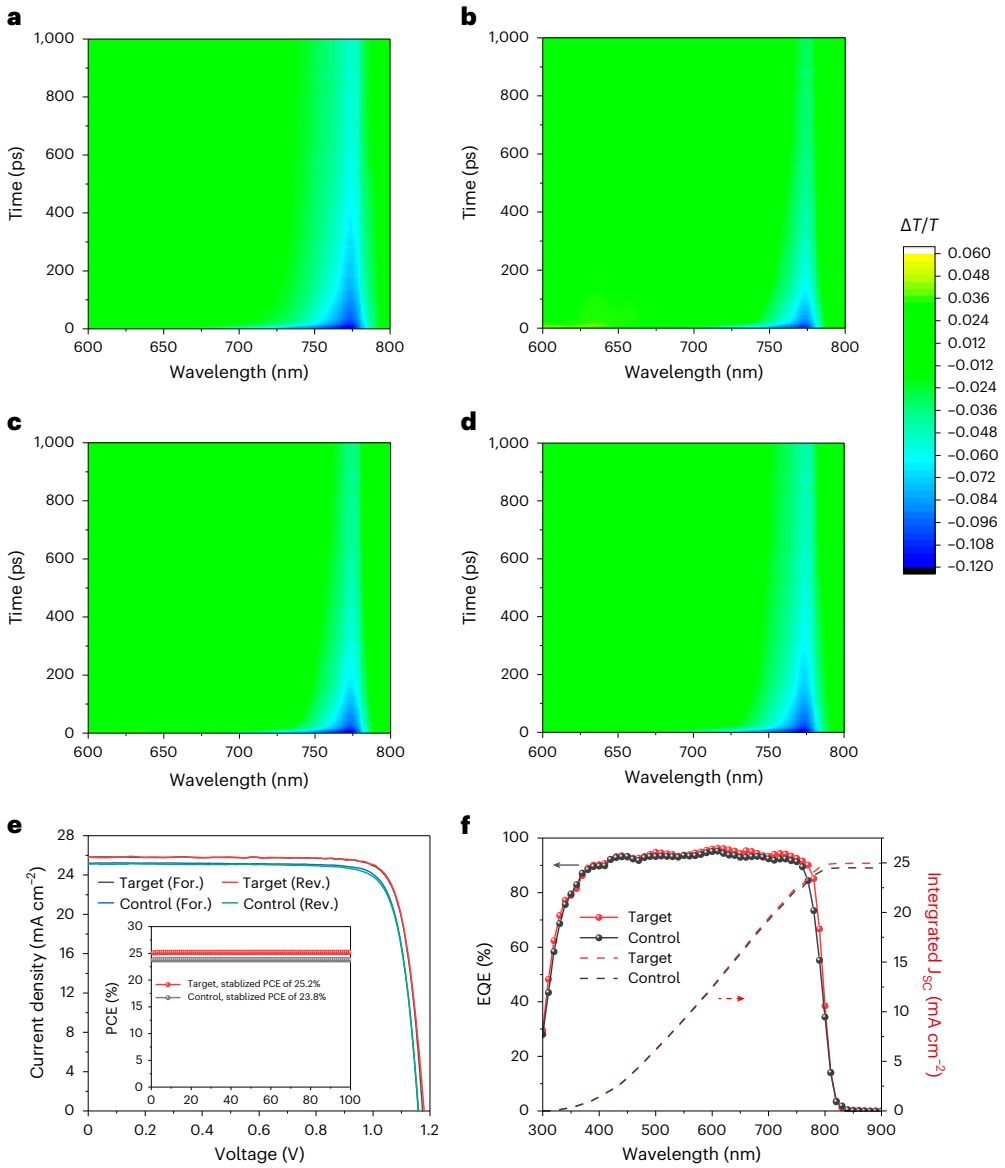

Fig. 2 | Characterization on carrier extraction and device performance. **a**–**d**, Dynamic decay curves of the absorption band for samples with different doping depths: control sample, 0 nm (**a**); target samples, 50 nm (**b**), 100 nm (**c**) and 20 nm (**d**). Excitation with a 120 fs light pulse of 420 nm wavelength with the power of 3.3 mW (5 kHz); $\Delta T/T$ represents the change of transmission after pump pulse. **e**, *J*–*V* curves of control and target devices under 1 sun illumination with cell size of 0.076 cm^2. For., forward; Rev., reverse. Inset: stabilized PCE at the maximum power point tracking. **f**, External quantum efficiency curve of control and target devices over 300 to 900 nm wavelengths, and their corresponding integrated J_{SC}.

region and an electron accumulation layer; the junction here therefore has a negligible rectification effect, which is considered as an ohmic contact. Here we studied the influence of the depletion region near the perovskite/HTL side on the performance and stability of the PSCs. According to the cross-section KPFM results in Fig. 1e, the potential change and the peak of the electric field (obtained by differentiating the potential curve) built into the control devices appeared at the heterointerface, suggesting that the depletion region was located at the heterointerface between the perovskite layer and the CTL. In contrast, the potential change and the peak of the electric field built into the target samples with a doping depth of 50 nm occurred inside the perovskite layer, which proved that the junction moved away from the heterointerface (Fig. 1f). For comparison, we also detected the location of the depletion region for the sample via traditional passivation. After surface passivation, the depletion region still locates at the heterointerface, similar to that of the control sample (Supplementary Fig. 18). The carrier concentrations of perovskite material and HTL were then tested by capacitance–voltage and Hall tests (Supplementary Figs. 19 and 20, and Supplementary Table 3), and the depletion region width was calculated accordingly. The results show that the theoretical calculation is consistent with the KPFM results (see Supplementary Note 2 for the detailed test and calculation processes, and Supplementary Table 4 for the related parameters).

Carrier extraction and photovoltaic performance

We then test the performance of control and target devices, and the photovoltaic parameters of the PSCs with different doping depths are summarized in Supplementary Table 5. The performance was affected by the doping depth and showed a maximum value at around 50 nm. According to the X-ray diffraction spectra, grazing-incidence wide-angle X-ray scattering results and scanning electron microscopy (SEM) images (Supplementary Figs. 22–24), the dopant did not affect the crystal structure, crystallinity and morphology of the perovskite material. The target sample showed smooth surface and cross-section

https://doi.org/10.1038/s41566-024-01383-5

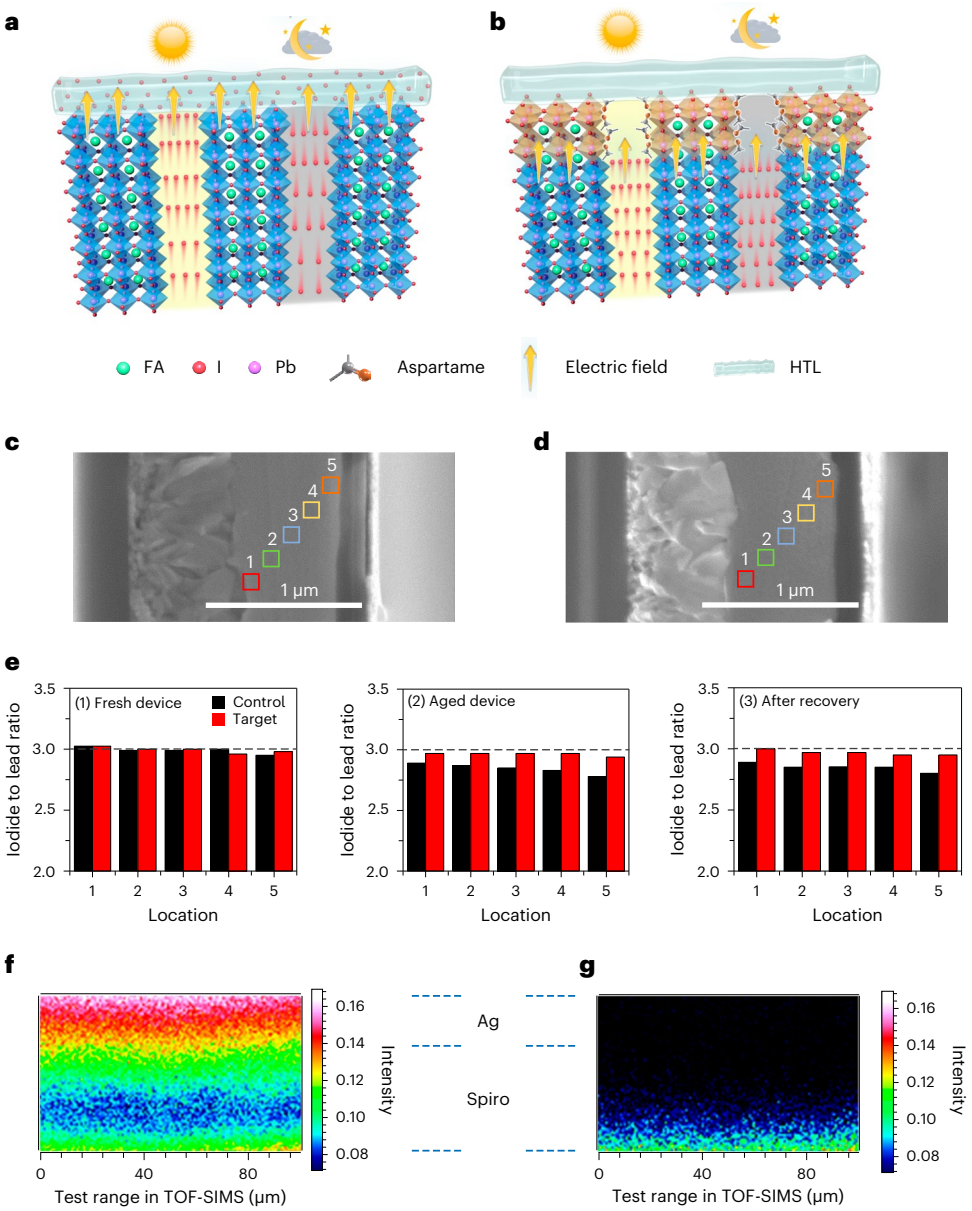

Fig. 3 | Effect of depletion region regulation on inhibition of iodide ion migration. a,**b**, Schematic diagram for inhibition of iodide ion migration in the control (**a**) and target (**b**) devices. **c**,**d**, Cross-section SEM images of control (**c**) and target (**d**) devices. Locations 1–5 mark the positions at which the EDX analyses were performed. **e**, The iodide to lead ratio in different regions of the perovskite film: (1) fresh device; (2) aged device (under illumination for 480 h); and (3) aged device after recovery. The horizontal dashed black lines represent the ideal stoichiometric iodide to lead ratio in the perovskite layer. **f**,**g**, Iodide distribution of 2D graphs in spiro-OMeTAD/Ag for the control (**f**) and target (**g**) samples. The samples were aged under continuous light soaking for 480 h. The colour bar represents the intensity of the iodide ions with arbitrary units.

morphology (Supplementary Fig. 25). We therefore inferred that the performance is related to the defect density in the depletion region. When the doping depth is shallow, there is higher defect density on the shallow surface than that inside perovskite layer[37], resulting in large recombination current in depletion region and thus poorer performance. As the doping depth deepens, the depletion region was moved inside the perovskite layer where defect density decreases sharply, leading to a champion PCE with optimal doping depth. However, when the doping depth is too deep, the PCE dropped because the extraction driving force of carriers nearby shallow surface will be weakened due to the small electric field intensity at the heterointerface, increasing the recombination chance. Time-resolved photoluminescence (TRPL) and transient absorption spectroscopy (TAS) were used to characterize the carrier extraction. The TRPL signals decay faster for PSCs with doping depth of around 50 nm than PSCs with other doping depth, indicating faster hole transfer rate into the HTL (Supplementary Fig. 26), which is consistent with the device performance. Further TAS experiments were performed to obtain details on the carrier dynamics[38–41]. As shown in Fig. 2a–d, the TAS spectra exhibited distinct ground-state bleaching (GSB) peaks at around 780 nm. For the HTL/perovskite stack, the faster that the non-equilibrium carriers are extracted, the faster the perovskite layer returns to the ground-state. The changes of GSB peak intensity with the delay time can therefore directly reflect the ability of HTL to extract holes. The GSB peak intensity of target sample is much weaker than the control one, indicating the faster carrier extraction (Fig. 2b). The ideality factors extracted from the illumination intensity dependence of the V_{OC} for target PSCs exhibited a value of 1.15 closer to 1 (Supplementary Fig. 27), which indicated a high-quality diode, consistent with the smaller leakage current (Supplementary Fig. 28). The recombination time constant (τ_r) derived from the transient

https://doi.org/10.1038/s41566-024-01383-5

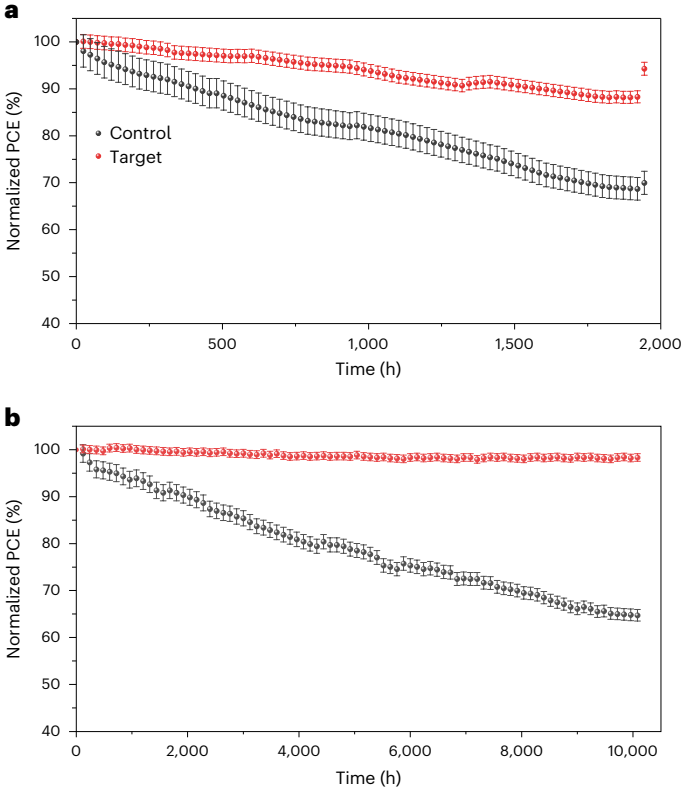

Fig. 4 | Stability test for target and control devices. Maximum power point tracking test was performed under 1 sun illumination (AM 1.5 G, 100 mW cm^{-2}). **a**, Perovskite solar cells under continuous MPP tracking conditions for 1,920 h. The PCE of the target (control) device dropped to 88.31 ± 1.29% (68.70 ± 2.41%) and returned to 94.29 ± 1.38% (69.98 ± 2.46%) of the initial value. **b**, Repeated 12 h light on/off cycles for over 10,000 h. The PCE of the target (control) device dropped to 98.35 ± 0.81% (64.73 ± 1.23%). The error bars denote s.d. for four individual devices.

photovoltage decays of the doped cells was substantially longer than that of the undoped one, which can be attributed to the lower charge recombination (Supplementary Fig. 29).

As a result, we achieved a champion PCE of 25.6% on 0.076 cm^2 solar cells using spiro-OMeTAD as HTL (Fig. 2e), with V_{OC} of 1.210 V, J_{SC} of 25.65 mA cm^{-2} and fill factor of 82.51% (certified 25.2%; Supplementary Fig. 30). The J_{SC} is in agreement with the integrated current density from external quantum efficiency (EQE) spectra in Fig. 2f. The EQE shows negligible difference at wavelengths shorter than 600 nm. At long wavelengths of around 700 to 800 nm, the EQE of the target device is larger than that of a control device, indicating a better carrier separation and extraction in the region near the perovskite/spiro-OMeTAD interface after regulating the depletion region. We also fabricated the 1 cm^2 solar cell to prove the scalability of our strategy (see Supplementary Fig. 31 and Supplementary Table 6). Moreover, this strategy enabled interface processing no longer affected by surface morphology and thus greatly enhanced reproducibility. The PCE distribution exhibited a narrow range of around 1%, which is comparable with silicon solar cells (Supplementary Fig. 32)[42].

Mechanism of ion migration inhibition

We further investigated the effect of depletion region regulation on the stability of the PSCs. Compared with the control device, the electric field width of the target device increased, but the intensity remained almost constant (Fig. 1e,f), which can be owned to larger potential drop induced by a better junction after regulating the depletion region. The electric field located in the perovskite layer with increased width and constant intensity would apply a larger force, directing from the HTL to the perovskite, to the iodide ions, which is helpful for confining iodide ion migration within the perovskite layer (Fig. 3a,b). We used energy-dispersive X-ray spectroscopy (EDX) to prove the effective suppression of ion migration; the spectrometer was equipped with a FlatQUAD detector at nanoscale resolution to study the iodide to lead ratio at five different depths inside of the PSCs under illumination (Fig. 3c–e). Figure 3e (1), (2) and (3) represent the iodide to lead ratio in different regions for a fresh device, an aged device, and an aged device post-recovery, respectively. The iodide to lead ratio in all regions of fresh perovskite film is ~3, as shown in Fig. 3e (1), showing good stoichiometric ratio. After ageing, we observed that the iodide to lead ratio clearly differed across the samples (Fig. 3e (2)). In the aged control device, the iodide to lead ratio decreases from locations 1 to 5, and the ratio is obviously smaller than 3.0, which indicates that the iodide ions strongly migrate to the interface and then diffuse into the HTL, and that the built-in electric field has a poor blocking effect on ion migration. In the aged target device, the iodide to lead ratio is ~3 across locations 1 to 4, and the ratio slightly decreases to around 2.9 at location 5. This is because the depletion region inside the perovskite layer successfully prevents iodide ions from approaching the heterointerface, and then the HTL and electrode. Moreover, the width of built-in electric field in perovskite layer is enhanced, which can extend the effective blocking range of the iodide ions. After the target device was kept in darkness overnight, the iodide to lead ratio almost returned to its initial state, but it could not be reversed in the control sample (Fig. 3e (3)) because the iodide ions had irreversibly entered the HTL and electrode. Through TOF-SIMS, we found that there are almost no iodide ions in the HTL and electrodes of the target samples after ageing. On the contrary, an obvious iodide signal can be detected in the HTL and electrode of control sample, which will be detrimental to its long-term operation stability (Fig. 3f,g and Supplementary Fig. 33).

Device stability

Due to the effective inhibition of iodide migration to the HTL and electrode, target devices exhibit excellent long-term stability. Here we used PTAA as the HTL in the stability test and the fresh PTAA device can achieve a certified PCE of 24.6% via depletion region regulation (Supplementary Fig. 34). The device maintained more than 88% of its initial efficiency after 1,920 h of continuous illumination under MPP operating conditions (65 °C at ambient air following ISOS-L-2) and returned to more than 94% of its initial efficiency after overnight recovery in darkness (Fig. 4a). The recovery of efficiency originated from the reversible iodide ion migration, which is consistent with the EDX results in Fig. 3e. By contrast, the control device showed little efficiency recovery due to the irreversible ion migration into the HTL and electrode. Furthermore, to simulate real working conditions, we kept the device in darkness for 12 h after every 12 h of continuous illumination (solar simulator/dark cycle at 65 °C and ambient air following ISOS-LC-2); it can still maintain 98% of the initial efficiency after 10,000 h (Fig. 4b). We also tested the stability for PSCs with different doping depths (Supplementary Fig. 35) and found that 50 nm was the optimal depth to simultaneously realize high performance and stability. The long-term stability can be slightly improved via a traditional passivation method. We further studied another two substances reported in the literature[33]—theophylline and theobromine. Both the PCE and the long-term stability have been greatly improved after the doping process, strongly demonstrating the effectiveness and universality of our strategy (Supplementary Figs. 36 and 37, and Supplementary Tables 7 and 8).

Online content

Any methods, additional references, Nature Portfolio reporting summaries, source data, extended data, supplementary information, acknowledgements, peer review information; details of author contributions and competing interests; and statements of data and code availability are available at https://doi.org/10.1038/s41566-024-01383-5.

References

1. Kojima, A., Teshima, K., Shirai, Y. & Miyasaka, T. Organometal halide perovskites as visible-light sensitizers for photovoltaic cells. *J. Am. Chem. Soc.* **131**, 6050–6051 (2009).
2. Kim, H.-S. et al. Lead iodide perovskite sensitized all-solid-state submicron thin film mesoscopic solar cell with efficiency exceeding 9%. *Sci. Rep.* **2**, 591 (2012).
3. Lee, M. M., Teuscher, J., Miyasaka, T., Murakami, T. N. & Snaith, H. J. Efficient hybrid solar cells based on meso-superstructured organometal halide perovskites. *Science* **338**, 643–647 (2012).
4. Burschka, J. et al. Sequential deposition as a route to high-performance perovskite-sensitized solar cells. *Nature* **499**, 316–319 (2013).
5. Jeon, N. J. et al. Solvent engineering for high-performance inorganic–organic hybrid perovskite solar cells. *Nat. Mater.* **13**, 897–903 (2014).
6. Chen, W. et al. Efficient and stable large-area perovskite solar cells with inorganic charge extraction layers. *Science* **350**, 944–948 (2015).
7. Park, J. et al. Controlled growth of perovskite layers with volatile alkylammonium chlorides. *Nature* **616**, 724–730 (2023).
8. *Best Research-Cell-Efficiency Chart* (NREL, 2023); https://www.nrel.gov/pv/cell-efficiency.html
9. Yuan, Y. & Huang, J. Ion migration in organometal trihalide perovskite and its impact on photovoltaic efficiency and stability. *Acc. Chem. Res.* **49**, 286–293 (2016).
10. Di Girolamo, D. et al. Ion migration-induced amorphization and phase segregation as a degradation mechanism in planar Perovskite solar cells. *Adv. Energy Mater.* **10**, 2000310 (2020).
11. Yuan, H. F. et al. Degradation of methylammonium lead iodide perovskite structures through light and electron beam driven ion migration. *J. Phys. Chem. Lett.* **7**, 561–566 (2016).
12. Domanski, K. et al. Migration of cations induces reversible performance losses over day/night cycling in perovskite solar cells. *Energy Environ. Sci.* **10**, 604–613 (2017).
13. Gottesman, R. et al. Photoinduced reversible structural transformations in free-standing $CH_3NH_3PbI_3$ perovskite films. *J. Phys. Chem. Lett.* **6**, 2332–2338 (2015).
14. Nie, W. et al. Light-activated photocurrent degradation and self-healing in perovskite solar cells. *Nat. Commun.* **7**, 11574 (2016).
15. Besleaga, C. et al. Iodine migration and degradation of perovskite solar cells enhanced by metallic electrodes. *J. Phys. Chem. Lett.* **7**, 5168–5175 (2016).
16. Zhao, Y. C. et al. Mobile-ion-induced degradation of organic hole-selective layers in perovskite solar cells. *J. Phys. Chem. C* **121**, 14517–14523 (2017).
17. Wang, Y. et al. Stabilizing heterostructures of soft perovskite semiconductors. *Science* **365**, 687–691 (2019).
18. Kato, Y. et al. Silver iodide formation in methyl ammonium lead iodide perovskite solar cells with silver top electrodes. *Adv. Mater. Inter.* **2**, 1500195 (2015).
19. De Bastiani, M. et al. Toward stable monolithic perovskite/silicon tandem photovoltaics: a six-month outdoor performance study in a hot and humid climate. *ACS Energy Lett.* **6**, 2944–2951 (2021).
20. Lin, D. X. et al. Ion migration accelerated reaction between oxygen and metal halide perovskites in light and its suppression by cesium incorporation. *Adv. Energy Mater.* **11**, 2002552 (2021).
21. Zhou, W. K. et al. Light-independent ionic transport in inorganic perovskite and ultrastable Cs-based perovskite solar cells. *J. Phys. Chem. Lett.* **8**, 4122–4128 (2017).
22. Wei, D. et al. Ion-migration inhibition by the cation–π interaction in perovskite materials for efficient and stable perovskite solar cells. *Adv. Mater.* **30**, 1707583 (2018).
23. Cai, Y. et al. Multifunctional enhancement for highly stable and efficient perovskite solar cells. *Adv. Funct. Mater.* **31**, 2005776 (2021).
24. Zai, H. et al. Sandwiched electrode buffer for efficient and stable perovskite solar cells with dual back surface fields. *Joule* **5**, 2148–2163 (2021).
25. Chen, C. et al. Arylammonium-assisted reduction of the open-circuit voltage deficit in wide-bandgap perovskite solar cells: the role of suppressed ion migration. *ACS Energy Lett.* **5**, 2560–2568 (2020).
26. Yang, S. et al. Stabilizing halide perovskite surfaces for solar cell operation with wide-bandgap lead oxysalts. *Science* **365**, 473–478 (2019).
27. Azmi, R. et al. Damp heat–stable perovskite solar cells with tailored-dimensionality 2D/3D heterojunctions. *Science* **376**, 73–77 (2022).
28. Cai, M. L. et al. Control of electrical potential distribution for high-performance perovskite solar cells. *Joule* **2**, 296–306 (2018).
29. Zhang, M. et al. Reconfiguration of interfacial energy band structure for high-performance inverted structure perovskite solar cells. *Nat. Commun.* **10**, 4593 (2019).
30. Wang, C. et al. Understanding and eliminating hysteresis for highly efficient planar perovskite solar cells. *Adv. Energy Mater.* **7**, 1700414 (2017).
31. Wang, Q. et al. Qualifying composition dependent p and n self-doping in $CH_3NH_3PbI_3$. *Appl. Phys. Lett.* **105**, 163508 (2014).
32. Yin, W. J., Shi, T. T. & Yan, Y. F. Unusual defect physics in $CH_3NH_3PbI_3$ perovskite solar cell absorber. *Appl. Phys. Lett.* **104**, 063903 (2014).
33. Wang, R. et al. Constructive molecular configurations for surface-defect passivation of perovskite photovoltaics. *Science* **366**, 1509–1513 (2019).
34. Andrade, J. S. Jr, Street, D. A., Shinohara, T., Shibusa, Y. & Arai, Y. Percolation disorder in viscous and nonviscous flow through porous media. *Phys. Rev. E* **51**, 5725–5731 (1995).
35. Oldenburg, C. M., Mukhopadhyay, S. & Cihan, A. On the use of Darcy's law and invasion-percolation approaches for modeling large-scale geologic carbon sequestration. *Greenh. Gases Sci. Technol.* **6**, 19–33 (2016).
36. Larson, R. G., Davis, H. T. & Scriven, L. E. Displacement of residual nonwetting fluid from porous media. *Chem. Eng. Sci.* **36**, 75–85 (1981).
37. Ni, Z. et al. Resolving spatial and energetic distributions of trap states in metal halide perovskite solar cells. *Science* **367**, 1352–1358 (2020).
38. Guo, Z. et al. Long-range hot-carrier transport in hybrid perovskites visualized by ultrafast microscopy. *Science* **356**, 59–62 (2017).
39. Xing, G. et al. Long-range balanced electron- and hole-transport lengths in organic–inorganic $CH_3NH_3PbI_3$. *Science* **342**, 344–347 (2013).
40. Giovanni, D. et al. Ultrafast long-range spin-funneling in solution-processed Ruddlesden–Popper halide perovskites. *Nat. Commun.* **10**, 3456 (2019).
41. Guo, Z., Manser, J. S., Wan, Y., Kamat, P. V. & Huang, L. B. Spatial and temporal imaging of long-range charge transport in perovskite thin films by ultrafast microscopy. *Nat. Commun.* **6**, 7471 (2015).
42. Lu, G. L., Zheng, F., Wang, J. Q. & Shen, W. Z. Thin Al_2O_3 passivated boron emitter of n-type bifacial c-Si solar cells with industrial process. *Prog. Photovoltaics* **25**, 280–290 (2017).

Methods

Materials

Lead iodide (PbI_2, 99.99%, trace metals basis) and 4-Isopropyl-4′-methyldiphenyliodonium tetrakis (pentafluorophenyl)borate (TPFB, 98%) were purchased from Tokyo Chemical Industry. Formamidinium iodide (FAI, 99%) was purchased from Advanced Election Technology. Deionized water, urea, hydrochloric acid (HCl, 37 wt% in water), thioglycolic acid (98%), $SnCl_2{\cdot}2H_2O$ (>99.995%), aspartame, alitame, *N*,*N*-dimethylmethanamide (DMF, anhydrous, 99.8%), spiro-OMeTAD, dimethyl sulfoxide (DMSO, anhydrous, 99.8%), IPA (anhydrous, 99.8%), lithium bis(trifluoromethanesulfonyl)imide (Li-TFSI), CB (anhydrous, 99.8%) and 4-*tert*-butylpyridine were purchased from Sigma-Aldrich and used without purification. Unless stated otherwise, all other materials such as methylammonium bromide (MABr) and PTAA were purchased from Xi'an Polymer Light Technology and used as received.

Perovskite solar cell fabrication

The FTO glasses were etched with zinc powder and 6 M HCl for 15 s to obtain patterned substrates. The patterned glasses were then sonicated with detergent, deionized water, ethanol and acetone for 15 min, respectively. After being cleaned and dried by N_2 flow, the substrates were treated with ultraviolet plasma for 30 min to remove the organic residues. The SnO_2 layer was prepared via a chemical bath deposition method used in another work[43]. The PbI_2 solution was prepared by dissolving 1.42 M PbI_2 into 1 ml DMF/DMSO mixed solvent (95:5/v:v). The solutions were stirred for at least 6 h before use. The FAI/MABr solution was prepared by dissolving 73 mg FAI and 3 mg MABr in 1 ml IPA. The PbI_2 solution was spin-coated on the substrate at 1,500 r.p.m. for 30 s, and then the FAI/MABr solution was spin-coated on the substrates at 1,700 r.p.m. for 30 s to form the precursor film. The precursor film is composed of small grains without a porous structure, as shown in Supplementary Fig. 3a. The precursor film was subsequently transferred outside of the glovebox and annealed in an ambient environment (relative humidity = 30%, 25 °C) to prepare the control sample[44]. The time to transfer the precursor film from a glovebox to an annealing hotplate is precisely controlled to 30 s, during which time the precursor film was exposed to the ambient environment. The films exhibited an obvious porous morphology that was different from that of the precursor, indicating that the humidity affected the structure of the perovskite precursor film during this short time (Supplementary Fig. 3b). The reason for the formation of a porous structure could be explained as follows: when exposed to the ambient environment, the disordered and loose structure of the grain boundaries—compared with that inside of the grains—make it easier for the water molecules in the ambient to penetrate inside the perovskite layers. Furthermore, the water molecules could weaken the bonding between the organic salts and the Pb–I cage, and may lead to some perovskite being decomposed into PbI_2 and FAI at the loose grain edge. Therefore, the decomposed grain boundaries by water molecules form the porous structure. For the target sample, it also took us 30 s to transfer precursor film from a glovebox to a spray table beside a hotplate at first. We then spent another 30 s spraying the dopant onto the precursor film surface. The morphology of the control and target samples is almost the same before thermal annealing (Supplementary Fig. 3b,c). The porous surface is convenient for dopant penetration and makes the doping process meeting the condition of Darcy's equation. The whole process is controlled within 1 min. Finally, the sample was transferred to the nearby hotplate for annealing at 150 °C for 15 min in ambient environment. The following preparation procedures of the HTL and electrode showed no difference for all devices: spiro-OMeTAD (75 mg ml^{-1} in CB) solution with 4-*tert*-butylpyridine and Li-TFSI doping was spin-coated at 3,000 r.p.m. as the HTL; finally, a 100-nm-thick silver counter electrode was deposited via thermal evaporation (under high vacuum with 1.0×10^{-4} Pa in a thermal evaporation system (JSD400)) and the evaporation rate was monitored by quartz crystal microbalances (FTM −106, Taiyao Vacuum Tech). All of these processes were conducted in a N_2-protected glovebox with O_2 and H_2O concentrations of less than 0.1 ppm.

Density functional theory calculations

First-principles calculations based on density functional theory (DFT) were carried out using the Vienna Ab initio Simulation Package for the further investigation of the interaction between the dopant and the perovskite material[45]. The generalized gradient approximation of Perdew–Burke–Ernzerhof functional was employed as the exchange-correlation functional[46]. We included dispersion corrections to the total energy using DFT-D3 scheme[47]. The plane-wave cutoff energy was set to 400 eV. The energy and force convergence criteria were set to 10^{-5} eV and 0.02 eV $Å^{-1}$, respectively. For geometry optimization, a $4 \times 4 \times 1$ k-point mesh was adopted for Brillouin-zone sampling. For self-consistent field calculation, $8 \times 8 \times 1$ *k*-point mesh was adopted for Brillouin-zone sampling. The surfaces were modelled by a slab consisting of 2×2 periodicity in the *a*–*b* plane and at least three atomic layers along the *c*-axis, separated by 15–20 Å of vacuum in the surface normal direction.

In our calculation process, the calculation model consists of $2 \times 2 \times 2$ $FAPbI_3$ unit cell with one defect site and one passivation molecule, and the most stable structure with the lowest energy is obtained. In detail, one C=O group is combined with an uncoordinated Pb^{2+}, and the binding energies were calculated as follows:

$$E_{\text{bind}} = E_{\text{sub+molecule}} - E_{\text{sub}} - E_{\text{molecule}}$$

$E_{\text{sub+molucule}}$, E_{sub} and E_{molecule} represent the energies of the substrate + molecule, the substrate, and the molecule, respectively. However, in actual perovskite crystals, the unit cell to defect site ratio is different. The molar mass and the density of the common $FAPbI_3$ are 636 g mol^{-1} and 4.10 g cm^{-3}, which means that there is around 10^{21} $FAPbI_3$ unit cells within 1 cm^3. The trap density for $FAPbI_3$ is around 10^{16} cm^{-3}. Therefore, in actual perovskite crystals, there is only one defect site among 10^5 $FAPbI_3$ unit cells, but such a calculation model cannot be achieved in the calculation process. In this case, the defect density in the calculation model is much higher than the actual defect density. The calculation results therefore exhibited relatively stronger binding energy.

Reporting summary

Further information on research design is available in the Nature Portfolio Reporting Summary linked to this article.

Data availability

The data that support the findings of this study are available from the corresponding authors on reasonable request.

References

43. Yoo, J. J. et al. Efficient perovskite solar cells via improved carrier management. *Nature* **590**, 587–593 (2021).
44. Zhao, Y. et al. Inactive $(PbI_2)_2RbCl$ stabilizes perovskite films for efficient solar cells. *Science* **377**, 531–534 (2022).
45. Kresse, G. & Furthmuller, J. Efficient iterative schemes for ab initio total-energy calculations using a plane-wave basis set. *Phys. Rev. B* **54**, 11169–11186 (1996).
46. Perdew, J. P., Burke, K. & Ernzerhof, M. Generalized gradient approximation made simple. *Phys. Rev. Lett.* **77**, 3865–3868 (1996).
47. Lee, K., Murray, E. D., Kong, L. Z., Lundqvist, B. I. & Langreth, D. C. Higher-accuracy van der Waals density functional. *Phys. Rev. B* **82**, 081101 (2010).

Acknowledgements

This work was supported by the National Key R&D Program of China (grant nos. 2020YFB1506400 and 2021YFB3800100) and the National Natural Science Foundation of China (grant nos.

U20A20245, U21A20171, 11834011 and 12074245). We thank H. Li, Q. Shan for KPFM measurements; R. Wang for TRPL measurements; J. Ding for TOF-SIMS measurements; X. Ding and N. Zhang for XPS and ultraviolet photoelectron spectroscopy measurements; B. Zhu for Fourier-transform infrared spectroscopy measurements; Q. Rao for X-ray diffraction measurements; and Z. Bao and Y. Lin for SEM measurement from the Instrumental Analysis Center of Shanghai Jiao Tong University. We thank X. Liu from the College of Arts and Sciences, University of Tokyo, for valuable advice on the experiments and paper.

Author contributions

Z.S., Q.H., Y.Y. and L.H. conceived the experiments, performed data analysis and wrote the paper. Z.S. led the fabrication of the solar cells. Y.S. and X.L. helped with the sample preparation for characterization. Y.W., Y.Y. and Y.Z. participated the discussion about the feasibility of the experiment. All authors discussed the results and commented on the paper. Q.H. and L.H. directed and supervised the entire research.

Competing interests

The authors declare no competing interests.

Additional information

Supplementary information The online version contains supplementary material available at https://doi.org/10.1038/s41566-024-01383-5.

Correspondence and requests for materials should be addressed to Qifeng Han, Yang Yang or Liyuan Han.

Peer review information *Nature Photonics* thanks Nam-Gyu Park, Michael Saliba and the other, anonymous, reviewer(s) for their contribution to the peer review of this work.

nature portfolio

Corresponding author(s): Qifeng Han, Yang Yang, Liyuan Han

Solar Cells Reporting Summary

Nature Portfolio wishes to improve the reproducibility of the work that we publish. This form is intended for publication with all accepted papers reporting the characterization of photovoltaic devices and provides structure for consistency and transparency in reporting. Some list items might not apply to an individual manuscript, but all fields must be completed for clarity.

For further information on Nature Research policies, including our data availability policy, see Authors & Referees.

Experimental design

Please check the following details are reported in the manuscript, and provide a brief description or explanation where applicable.

1. Dimensions

Area of the tested solar cells	☒ Yes ☐ No	The aperture area was 0.0763 cm2 . *Explain why this information is not reported/not relevant.*
Method used to determine the device area	☒ Yes ☐ No	Black metal aperture masks were used during the J-V measurements. *Explain why this information is not reported/not relevant.*

2. Current-voltage characterization

Current density-voltage (J-V) plots in both forward and backward direction	☒ Yes ☐ No	Provided in this manuscript.
Voltage scan conditions	☒ Yes ☐ No	Provided in Characterization Section of Supplementary Information. *Explain why this information is not reported/not relevant.*
Test environment	☒ Yes ☐ No	Provided in this manuscript. *Explain why this information is not reported/not relevant.*
Protocol for preconditioning of the device before its characterization	☐ Yes ☒ No	No preconditioning protocol was applied before characterization. *Explain why this information is not reported/not relevant.*
Stability of the J-V characteristic	☒ Yes ☐ No	Stabilized PCEs were provided. *Explain why this information is not reported/not relevant.*

3. Hysteresis or any other unusual behaviour

Description of the unusual behaviour observed during the characterization	☐ Yes ☒ No	No unusual behavior was observed. *Explain why this information is not reported/not relevant.*
Related experimental data	☐ Yes ☒ No	No unusual behavior was observed. *Explain why this information is not reported/not relevant.*

4. Efficiency

External quantum efficiency (EQE) or incident photons to current efficiency (IPCE)	☒ Yes ☐ No	External quantum efficiency (EQE) was provided. *Explain why this information is not reported/not relevant.*
A comparison between the integrated response under the standard reference spectrum and the response measure under the simulator	☒ Yes ☐ No	The integrated Jsc values from QE were consistent with Jsc values from J-V measurements. *Explain why this information is not reported/not relevant.*

For tandem solar cells, the bias illumination and bias voltage used for each subcell

☐ Yes
☒ No

This is not a research about tandem solar cell.

Explain why this information is not reported/not relevant.

5. Calibration

Light source and reference cell or sensor used for the characterization

☒ Yes
☐ No

Provided in Characterization Section of Supplementary Information.

Explain why this information is not reported/not relevant.

Confirmation that the reference cell was calibrated and certified

☒ Yes
☐ No

The reference cell was calibrated by AIST.

Explain why this information is not reported/not relevant.

Calculation of spectral mismatch between the reference cell and the devices under test

☒ Yes
☐ No

The mismatch factor is 0.9793 in the certification report.

Explain why this information is not reported/not relevant.

6. Mask/aperture

Size of the mask/aperture used during testing

☒ Yes
☐ No

The aperture area was 0.0763 cm2.

Explain why this information is not reported/not relevant.

Variation of the measured short-circuit current density with the mask/aperture area

☐ Yes
☒ No

We measured the short-circuit current density with identical masks.

Explain why this information is not reported/not relevant.

7. Performance certification

Identity of the independent certification laboratory that confirmed the photovoltaic performance

☒ Yes
☐ No

Test and Calibration Center of New Energy Device and Module, Shanghai Institute of Microsystem and Information Technology, Chinese Academy of Sciences (SIMIT).

Explain why this information is not reported/not relevant.

A copy of any certificate(s)

☒ Yes
☐ No

The certification report can be found in Supplementary Fig. 30 and 34.

Explain why this information is not reported/not relevant.

8. Statistics

Number of solar cells tested

☒ Yes
☐ No

Provided in the manuscript.

Explain why this information is not reported/not relevant.

Statistical analysis of the device performance

☒ Yes
☐ No

Provided in the manuscript.

Explain why this information is not reported/not relevant.

9. Long-term stability analysis

Type of analysis, bias conditions and environmental conditions

☒ Yes
☐ No

Provided in this manuscript and Characterization section of Supplementary Information.

Explain why this information is not reported/not relevant.